OPEN ACCESS

remote sensing

ISSN 2072-4292

www.mdpi.com/journal/remotesensing

Supplementary Information

Spaceborne Mine Waste Mineralogy Monitoring in South Africa, Applications for Modern Push-Broom Missions: Hyperion/OLI and EnMAP/Sentinel-2. *Remote Sens*. 2014, *6*, 6790-6816

Christian Mielke [1,2,*], Nina Kristine Boesche [1,2], Christian Rogass [1], Hermann Kaufmann [1], Christoph Gauert [3] and Maarten de Wit [4]

1. Helmholtz Centre Potsdam, German Research Centre for Geosciences, Telegrafenberg, 14473 Potsdam, Germany; E-Mails: nina.boesche@gfz-potsdam.de (N.K.B.); christian.rogass@gfz-potsdam.de (C.R.); hermann.kaufmann@gfz-potsdam.de (H.K.)
2. Institut für Erd- und Umweltwissenschaften, Universität Potsdam, 14476 Potsdam-Golm, Germany
3. Department of Geology, University of the Free State (UFS), Bloemfontein, South Africa; E-Mail: gauertcdk@ufs.ac.za (C.G.)
4. Africa Earth Observatory Network (AEON), Nelson Mandela Metropolitain University, Summerstrand, Port Elizabeth, South Africa; E-Mail: maarten.dewit@nmmu.ac.za (M.d.W.)

* Author to whom correspondence should be addressed; E-Mail: christian.mielke@gfz-potsdam.de; Tel.: +49-331-288-1763; Fax: +49-331-288-1192.

Supplementary Material

Data from additional analysis and clarifications to the processing workflow are presented here as additional material to help readers of the article to better understand the processing methodology that otherwise would have had to be omitted to preserve the integrity and compactness of the article.

List of Abbreviations

This list should remind the reader of the abbreviations used throughout the text.

Abbreviation	Meaning
AEON	Africa Earth Observatory Network
ALI	Advanced Land Imager (multispectral spaceborne sensor)
AMD	acid mine drainage
ASTER	Advanced Spaceborne Thermal Emission and Reflection Radiometer (multispectral spaceborne sensor)
BMWi	Department of Economics and Technology (Germany)

EeteS	EnMAP end-to-end Simulation
EnMAP	Environmental Mapping and Analysis Program, (German hyperspectral satellite mission)
EO-1	Earth Observing-1 Satellite, with ALI and Hyperion instruments
ESA	European Space Agency
ETM+	Enhanced Thematic Mapper Plus (multispectral spaceborne sensor)
FWHM	full width at half maximum
Ga	giga years
IFD	iron feature depth
LMI	Layered Mafic Intrusion
MME	mean model error
MICA	Material Identification and Characterization Algorithm
MSSIM	mean structural similarity index measure
NASA	National Aeronautics and Space Administration
NIR	Near Infrared
OLI	Operational Land Imager (multispectral spaceborne sensor)
TOAREF	top of the atmosphere reflectance (at sensor reflectance)
PGE	platinum group elements
SPY	Spectral Python
SRF	Spectral Response Function
SWIR1	Short Wave Infrared 1
SWIR2	Short Wave Infrared 2
UFS	University of the Free State
UG2	Upper Group 2 Reef
USGS	United States Geological Survey
VNIR	visible and near-infrared
XRD	X-ray diffraction
XRF	X-ray fluorescence

Supplement 1

The shoulder positions listed in Table S1 represent averages of the TETRACORDER shoulder definition, which uses a wavelength range for the definition of the left and right shoulder of the absorption feature to minimize the influence of noise in the spectrum [S1]. Mineral formulas are after Anthony *et al*. [S2].

Table S1. Spectra from the USGS digital spectral library of iron-bearing minerals and materials and their characteristic absorption features that were used for the comparison of the different multispectral sensors. The entries are grouped into three groups: Iron Oxides (Fe-oxides), Mine Waste (M. Waste) and Pyroxene.

Feature Number	USGS Reference Spectra Name	Left Shoulder Average (nm)	Right Shoulder Average (nm)	Group	Formula of Dominant Mineral
0	Hematite FE2602	755	1,076	Fe-oxides	α–Fe_2O_3
1	Hematite HS45.3	751	1,060	Fe-oxides	α–Fe_2O_3
2	Hematite WS161	755	1,076	Fe-oxides	α–Fe_2O_3
3	Hematite GDS27	755	1,244	Fe-oxides	α–Fe_2O_3
4	Hematite_Thin_Film	742	1,222	Fe-oxides	α–Fe_2O_3
5	Goethite WS222	751	1,060	Fe-oxides	α–$Fe^{3+}O(OH)$
6	Goeth + qtz.5 + Jarosite.5	722	1,281	M. Waste	α–$Fe^{3+}O(OH)$
7	Schwertmannite BZ93-1	761	1,293	M. Waste	$Fe_{16}{}^{3+}O_{16}(SO_4)_2(OH)_{12}{\bullet}nH_2O$(n~10 to 12)
8	Acid_Mine_Dr Assemb1-Fe3+	788	1,293	M. Waste	Not Available
9	Acid_Mine_Dr Assemb2-Fe3+	757	1,231	M. Waste	Not Available
10	Jarosite GDS99	713	1,292	M. Waste	$Fe_3{}^{3+}(SO4)_2(OH)_6$
11	Fe-Hydroxide	779	1,230	M. Waste	$Fe^{3+}(OH)_3$
12	Ferrihydrite GDS75 Syn	792	1,039	M. Waste	$Fe_2O_3{\bullet}9H_2O$
13	Butlerite GDS25	792	1,039	M. Waste	$Fe^{3+}(SO_4)(OH){\bullet}2H_2O$
14	Hypersthene	750	1,065	Pyroxene	$(Mg,Fe)Si_2O_6$
15	Diopside NMNHR18685	701	1,301	Pyroxene	$(Ca,Mg)Si_2O_6$
16	Jadeite HS343.3B	890	1,232	Pyroxene	$Na(Al,Fe^{3+})Si_2O_6$
17	Pigeonite HS199.3B	802	1,232	Pyroxene	$(Mg,Fe^{2+},Ca)(Mg,Fe^{2+})Si_2O_6$
18	Bronzite HS9.3B	715	1,215	Pyroxene	$(Mg,Fe)Si_2O_6$

Supplement 2

Field sampling scheme (Figure S1), showing the layout of the 17 test surfaces at each test site in Figures 2 and 3. This scheme was used at a scale of 90 × 90 m, which represents the ground sampling distance (GSD) of Hyperion, EnMAP, OLI, ETM+ and ALI.

Figure S1. Point spread function (PSF) adapted field sampling scheme.

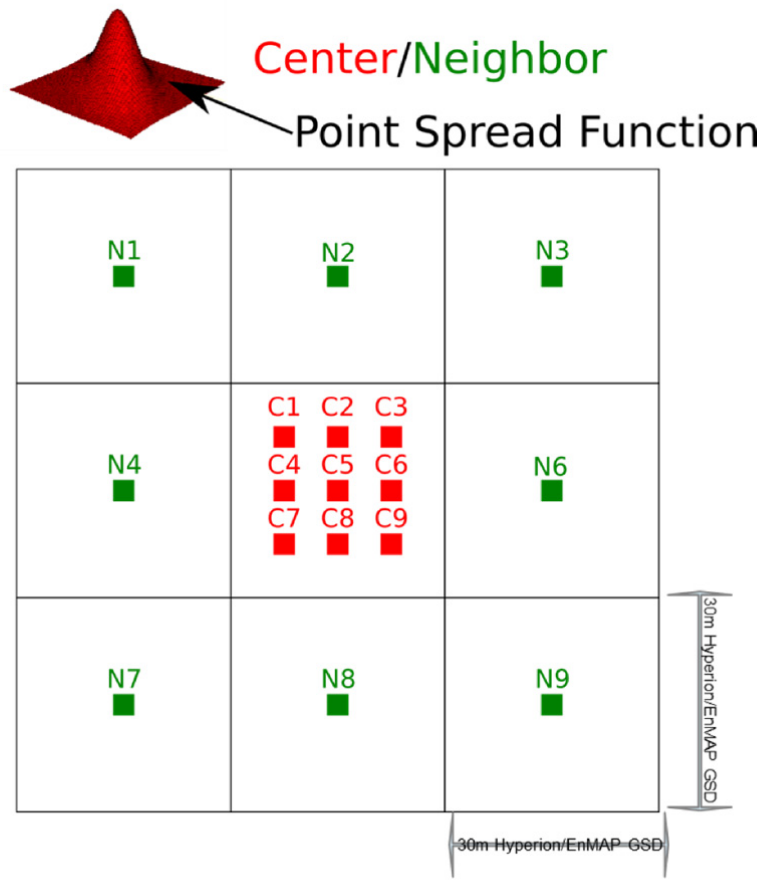

Supplement 3

The mean structural similarity index measure (MSSIM) from Wang *et al.* [S3], implemented in scikit-image [S4], was calculated as a quantitative measure for the similarity of the image content of two images. The MSSIM was selected as quality indicator, because it represents a sensitive image-based measure to detect subtle changes between similar images, such as image noise, contrast and brightness changes, which can be induced by spectral resampling, interpolation or by different processing techniques. The SSIM is calculated in a local moving window, w1 and w2 in the images, I1 and I2, of a square size of 11 × 11 pixel, according to the Equation (1) from Wang *et al.* [S3], with μ_{w1} being the average in Window 1, μ_{w2} being the average in Window 2, σ_{w1}^2 the variance in Window 1, σ_{w2}^2 the variance in Window 2 and σ_{w1w2} the covariance of w1 and w2. Additionally, the following parameters are $c_1= (K_1L)^2$ and $c_2 = (K_2L)^2$ with L representing the dynamic range of the pixel values and $K_1 = 0.01$ and $K_2 = 0.03$ as implemented in the scikit-image [S4] source code. The MSSIM is then defined according to Equation S2 [S3]. Figure S2 shows the processing workflow in which the MSSIM was used.

$$\mathrm{SSIM}\ (w_1,w_2) = ([2 *\mu_{w1}*\mu_{w2}+ c_1]*[2*\sigma_{w1w2}+ c_2])/([\ \mu_{w1}^2+\mu_{w2}^2+ c_1]*[\ \sigma_{w1}^2+ \sigma_{w2}^2+ c_2]) \quad (1)$$

$$\mathrm{MSSIM}\ (w_1,w_2) = \frac{1}{M}\sum_{j=1}^{M} \mathrm{SSIM}(w1, w2) \quad (2)$$

Figure S2. Processing schemes to illustrate the workflows in which the MSSIM was used as a comparator for the image data.

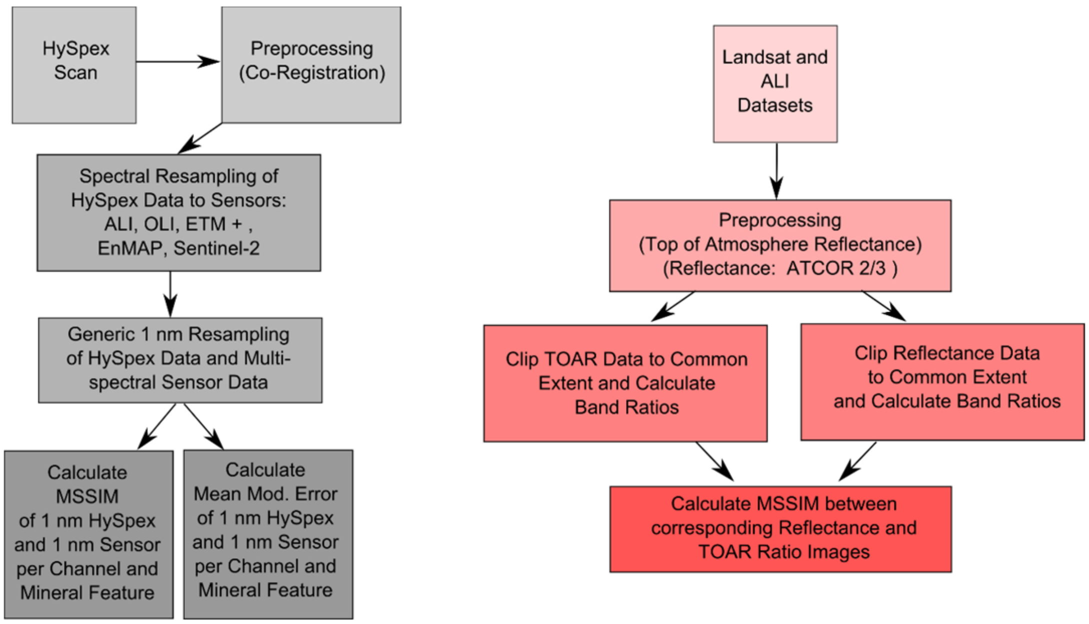

Supplement 4

Iron feature depth (IFD) calculated from primary (Figure S3) and secondary iron-bearing minerals (Figure S4) of spectra from the USGS digital spectral library [S5]. Please note the large IFD values of bronzite in Figure S3 and Jarosite in Figure S4 compared to all of the other iron bearing minerals in the respective diagrams.

Figure S3. Iron feature depth (IFD) values calculated from primary iron-bearing minerals calculated from the USGS digital spectral library.

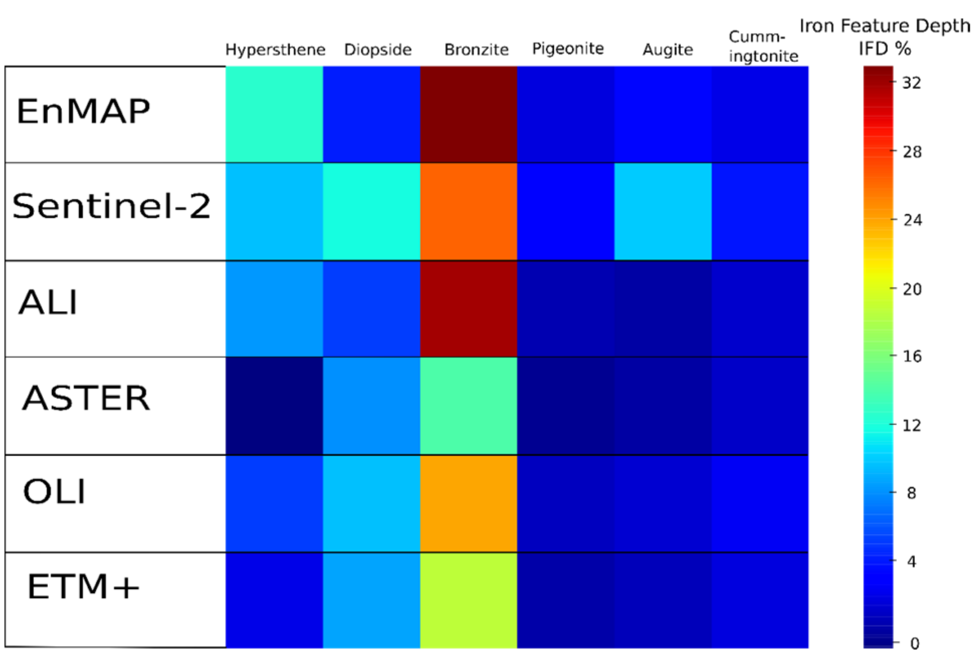

Figure S4. Iron feature depth (IFD) values calculated from secondary iron-bearing minerals calculated from the USGS digital spectral library. Acid mine drainage spectra are labeled as AMD.

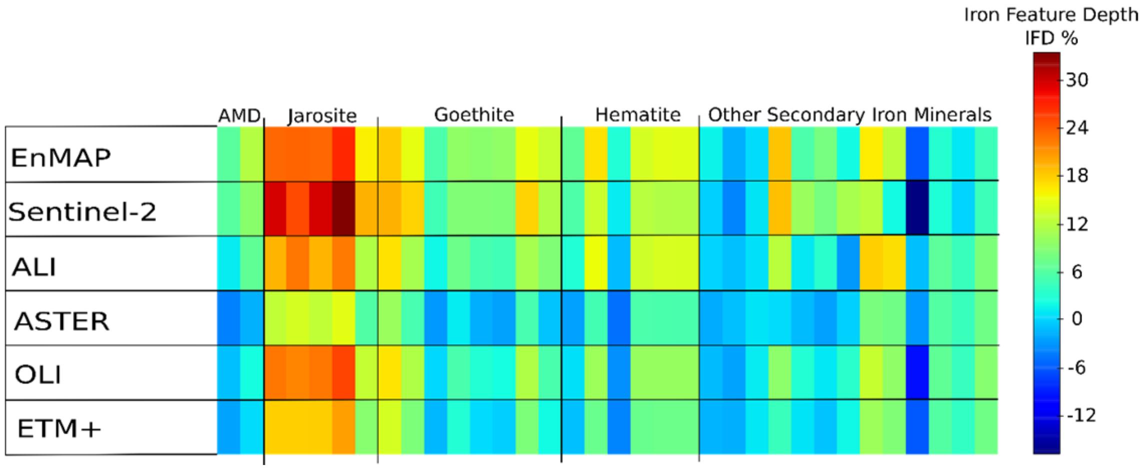

Supplement 5

Here, spectrally resampled field data illustrate how the abundance of vegetation on the test site alters the iron absorption feature at 900 nm and, hence, impacts on the iron feature depth. They also show the need for hyperspectral data when mixtures of PGE tailing material and vegetation need to be considered. Sentinel-2 in Figure S5 is still able to show the small impact of the iron feature on the vegetation spectrum, whilst OLI fails completely at this task as shown in Figure S6.

Figure S5. Iron feature depth (IFD) calculated from the resampled *in situ* ASD field-spectrometer measurements of the spill site: EnMAP (**left**) and Sentinel-2 (**right**). Please note the change in the iron absorption feature. Spectra are offset by 0.05 for clarity.

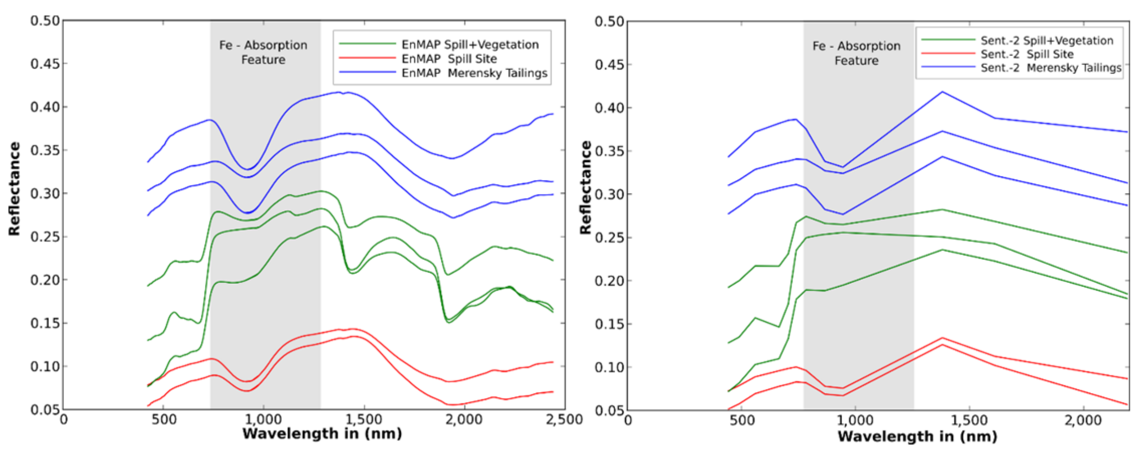

Figure S6. IFD calculated from the resampled *in situ* ASD field-spectrometer measurements of the spill site: Hyperion (**left**) and OLI (**right**). Please note the change in the iron absorption feature. Please note that mixtures of tailings material with vegetation are only detectable with Hyperion. Spectra are offset by 0.05 for clarity.

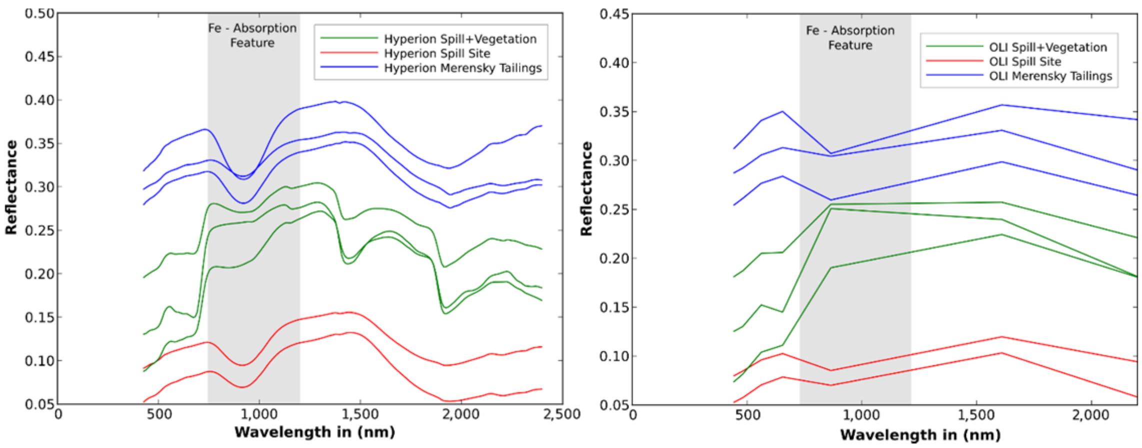

References

S1. Clark, R.N.; Swayze, G.A.; Livo, K.E.; Kokaly, R.F.; Sutley, S.J.; Dalton, J.B.; McDougal, R.R.; Gent, C.A. Imaging spectroscopy: Earth and planetary remote sensing with the USGS Tetracorder and expert systems. *J. Geophys. Res.: Planets* **2003**, *108*, doi:10.1029/2002JE001847.

S2. *Handbook of Mineralogy*; Anthony, J.W.; Bideaux, R.A.; Bladh, K.W.; Nichols, M.C., Eds.; Mineralogical Society of America: Chantilly, VA, USA, 2004.

S3. Wang, Z.; Bovik, A.C.; Sheikh, H.R.; Simoncelli, E.P. Image quality assessment: From error visibility to structural similarity. *IEEE Trans. Image Process.* **2004**, *13*, 600–612.

S4. Van der Walt, S.; Schoenberger, J.L.; Nunez-Iglesias, J.; Boulonge, F.; Warner, J.D.; Yager, N.; Gouillart, E.; Yu, T. scikit-image: Image processing in Python. *PeerJ* **2014**, *2*, e336v2. Available online: https://peerj.com/preprints/336v2/ (accessed on 17 April 2014).

S5. Clark, R.N.; Swayze, G.A.; Wise, R.; Livo, E.; Hoefen, T.M.; Kokaly, R.F.; Sutley, S.J. *USGS Digital Spectral Library Splib06a*; Geological Survey (U.S.) Clark, Ed.; U.S. Geological Survey Data Series; Rev. Sept. 20, 2007; U.S. Geological Survey: Denver, CO, USA, 2007.